Mechanisms of fatigue crack initiation and propagation in auxetic meta-biomaterials

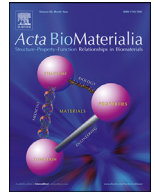Kolken, H. M.A.; Garcia, A. Fontecha; Plessis, A. Du; Meynen, A.; Rans, C.; Scheys, L.; Mirzaali, M. J.; Zadpoor, A. A.

Important note
To cite this publication, please use the final published version (if applicable).
Please check the document version above.

Full length article

Mechanisms of fatigue crack initiation and propagation in auxetic meta-biomaterials

H.M.A. Kolken [a,*], A. Fontecha Garcia [b], A. Du Plessis [c], A. Meynen [d], C. Rans [e], L. Scheys [d,f], M.J. Mirzaali [a], A.A. Zadpoor [a]

[a] Department of Biomechanical Engineering, Delft University of Technology, Delft, Netherlands
[b] 3D Systems – LayerWise NV, Leuven, Belgium
[c] Research group 3D Innovation, Stellenbosch University, Stellenbosch, South-Africa
[d] U Leuven, Institute for Orthopedic Research and Training, Leuven, Belgium
[e] Department of Aerospace Structures and Materials, Delft University of Technology, Delft, Netherlands
[f] Division of Orthopedics, University Hospitals Leuven, Belgium

ARTICLE INFO

ABSTRACT

The fatigue performance of additively manufactured auxetic meta-biomaterials made from commercially pure titanium has been studied only recently. While certain assumptions have been made regarding the mechanisms underlying their fatigue failure, the exact mechanisms are not researched yet. Here, we studied the mechanisms of crack formation and propagation in cyclically loaded auxetic meta-biomaterials. Twelve different designs were subjected to compression-compression fatigue testing while performing full-field strain measurement using digital image correlation (DIC). The fatigue tests were stopped at different points before complete specimen failure to study the evolution of damage in the micro-architecture of the specimens using micro-computed tomography (micro-CT). Furthermore, finite element models were made to study the presence of stress concentrations. Structural weak spots were found in the inverted nodes and the vertical struts located along the outer rim of the specimens, matching the maximum principal strain concentrations and fracture sites in the DIC and micro-CT data. Cracks were often found to originate from internal void spaces or from sites susceptible to mode-I cracking. Many specimens maintained their structural integrity and exhibited no signs of rapid strain accumulation despite the presence of substantial crack growth. This observation underlines the importance of such microscale studies to identify accumulated damage that otherwise goes unnoticed. The potential release of powder particles from damaged lattices could elicit a foreign body response, adversely affecting the implant success. Finding the right failure criterion, therefore, requires more data than only those pertaining to macroscopic measurements and should always include damage assessment at the microscale.

Statement of significance

The negative Poisson's ratio of auxetic meta-biomaterials makes them expand laterally in response to axial tension. This extraordinary property has great potential in the field of orthopedics, where it could enhance bone-implant contact. The fatigue performance of additively manufactured auxetic meta-biomaterials has only recently been studied and was found to be superior to many other bending- and stretch-dominated micro-architectures. In this study, we go beyond these macroscopic measurements and focus on the crack initiation and propagation. Full-field strain measurements and 3D imaging are used to paint a detailed picture of the mechanisms underlying fatigue. Using these data, specific aspects of the design and/or printing process can be targeted to improve the performance of auxetic meta-biomaterials in load-bearing applications.

---

* Corresponding author.
E-mail address: h.m.a.kolken@tudelft.nl (H.M.A. Kolken).

1. Introduction

Architected materials have attracted much attention recently. With the advances in additive manufacturing (AM), it has now become possible to manufacture these complex, micro-architected three-dimensional structures. The concept of metamaterials is built on the idea that "function follows form" and that the macroscale properties of such materials are primarily determined by their small-scale geometrical design [1]. The concept of meta-materials is also applicable in biology and medicine where the micro-architecture of so-called "meta-biomaterials" is optimized to achieve a unique combination of mechanical, mass-transport, and biological properties, thereby improving the long-term performance of bone implants [1–3].

Here, we focus on a specific class of meta-biomaterials that expands laterally in response to axial stretch. These materials are collectively referred to as auxetic meta-biomaterials, of which first proof dates back to the 1870s [4]. They have not only been studied for their negative Poisson's ratio (NPR), but also for their potential in exhibiting high levels of indentation resistance, shear resistance, energy dissipation, and fracture toughness [5–7]. The benefits of auxetic meta-biomaterials for improving the performance of medical devices and procedures have been demonstrated before [3]. For example, combining auxetic and non-auxetic meta-biomaterials has been shown to improve the bone-implant contact in hip stems that are subjected to bending. The lateral side of such implants experiences tension. A non-auxetic material (most solids) would contract under tension, which will adversely affect the bone-implant contact. With the lateral application of an auxetic meta-biomaterial, the implant-bone contact could be improved, thereby enhancing bony ingrowth, strengthening the mechanical fixation of the implant, and decreasing the risk of aseptic loosening [3,8]. The latter is associated with the mechanical failure of the implant-bone interface and is the most prevalent failure mode in total hip replacements [9,10].

The morphological and *quasi-static* mechanical properties of Ti-6Al-4 V auxetic meta-biomaterials have been assessed before, and were deemed appropriate for bone implant applications [11]. In load-bearing settings, however, meta-biomaterials will be subjected to cyclic loading as well, which underlines the importance of studying their fatigue performance. Until recently, no experimental data was available on the fatigue performance of auxetic meta-biomaterials that are additively manufactured from metals and are, thus, appropriate for application as load-bearing orthopedic implants. We addressed this lack of data in an extensive study of the compression-compression fatigue behavior of AM auxetic meta-biomaterials made from commercially pure titanium (CP-Ti) [12]. CP-Ti is known for its excellent fatigue resistance, probably as a result of its ductility, which would slow down crack initiation and propagation [13–15]. With an average maximum design stress of $0.47\sigma_y$ at 10^6 cycles, the auxetic specimens showed an unusually high level of fatigue performance [12]. Some of the high-density designs even surpassed the limit of topology-optimized structures that were designed for optimal fatigue performance [12]. Other studies also confirmed that auxetic meta-biomaterials generally outperform their non-auxetic counterparts in terms of fatigue strength, irrespective of the material type [12,16,17]. Post-test examinations showed that cracks were mainly formed around the strut junctions, while cracks were assumed to originate from the internal void spaces [12].

Here, we study the initiation and propagation of macroscale cracks in metallic auxetic meta-biomaterials during compression-compression fatigue testing. We used the exact same unit cell designs (A-D) as in our previous study to build AM CP-Ti cylindrical specimens with three different values of the relative density (RD) [12]. Finite element (FE) models were created to assess the location of stress concentrations inside the structures under compression. During the fatigue tests, full-field strain measurements were performed using digital image correlation (DIC). The specimens were tested till 25% or 50% of their maximum number of cycles to assess the macrostructural changes over time. Detailed 3D models of the internal micro-architecture of tested specimens were constructed using micro-computed tomography (micro-CT). The collected data was then used to paint a detailed picture of the mechanisms underlying fatigue in metallic auxetic meta-biomaterials.

2. Materials and methods

2.1. Design and additive manufacturing of auxetic meta-biomaterials

In continuation of and similar to the previous study on this topic [12], we used four different unit cell types (A-D) based on the re-entrant hexagonal honeycomb with an aspect ratio (*a/b*) of 1.0 (A-B) and 1.5 (C-D) (Fig. 1). Each aspect ratio was fitted with two unique re-entrant angles (θ) of 10°, 15°, 20°, and 25°, for A-D respectively. The four unit cell types were used to build cylindrical specimens (Ø 25 mm and $h \approx 37.5$ mm) with three different values of the relative density (RD) (*i.e.*, $\approx$ 5%, $\approx$ 25%, and $\approx$ 45%) (Table 1). The relative density values of design D slightly deviated from the aforementioned values, due to a fault in the design software, as mentioned in [12]. All twelve designs were manufactured using the same methodology as presented earlier [12]. Briefly, the specimens were built on a DMP Flex 350 machine with DMP Control Software (3D Systems, Leuven, Belgium) using Ti Gr1 (CP-Ti) powder (Fig. 1). Five specimens were printed for each respective design and all specimens were manually removed from the build plate. Excess powder particles were removed in an ultrasonic bath while the specimens were immersed in 96% ethanol.

2.2. Morphological characterization

Once manufactured, the specimens were visually inspected to assess their print quality. Similar to the specimens used in our previous study [12], the structures with a relatively high density exhibited signs of warping. Both ends of the cylinder were, therefore, turned on a lathe, to make sure the compression plates would be in full contact during fatigue testing. The dimensions of the specimens were measured using a caliper, while a laboratory scale (Sartorius AG, Göttingen, Germany, 0.1 mg accuracy) was used to weigh the specimens. Subsequently, the dry weighing technique was used to determine the as-manufactured relative density of the specimens. The weight of the specimens was, therefore, divided by the weight of a solid CP-Ti object with similar dimensions and a density of 4.51 g/cm³ [18].

2.3. Finite element modeling

The loading of the auxetic meta-biomaterials was simulated using FE models, which were developed to investigate the presence of stress concentrations affecting their compression-compression fatigue behavior. Three-dimensional models of each structure were converted to finite element meshes in ANSA (v19.1, BETA CAE Systems, Thessaloniki, Greece). All simulations were performed using the implicit solver of Abaqus (v2017, Dassault Systemes, Vélizy-Villacoublay, France). A convergence study was used to determine the appropriate element size. Each model consisted of approximately six million quadratic tetrahedral (C3D10) elements. A smaller element size was required to mesh design C, which increased the number of tetrahedral elements in the model. Isotropic
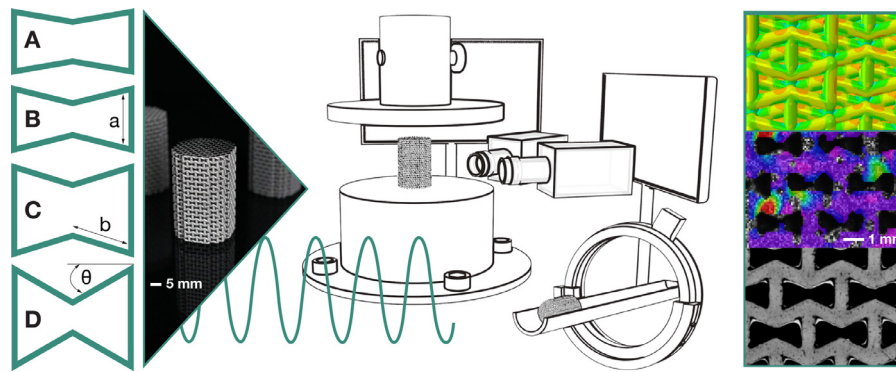
Fig. 1. The study outline showing the four different design types: A, B, C, and D, their translation to AM, three-dimensional CP-Ti specimens, and their assessment using finite element modeling, compression-compression fatigue testing, digital image correlation and micro-CT scanning.

elastic material properties were assigned to the meshes with an elastic modulus of 110 GPa and a Poisson's ratio of 0.3. The model was complimented with plastic properties that were derived from a uniaxial tensile stress test, performed by 3D Systems. Due to convergence issues, these properties could only be implemented up to the point where necking commenced. A vertical displacement, corresponding to $0.5\sigma_y$ (unique for every design) in the experiments, was applied to the top nodes of each structure while their lateral movements were constrained. The bottom nodes were constrained in all directions. The calculated stress concentrations were visually inspected and were compared to the experimental fracture points. To study the differences in stress concentrations between the designs, the low-density models of design A, B, C and D (RD $\approx$ 5%) were subjected to a vertical displacement of 0.5 mm. The mean absolute maximum principal stress was calculated at the location of stress concentrations, based on five unique data points, to gain insight in the differences between the designs.

2.4. Mechanical testing

Before we could assess the initiation and propagation of fatigue cracks in these auxetic meta-biomaterials, we first had to verify their *quasi-static* mechanical properties. Three specimens of each design were, therefore, preloaded (5 N) and axially compressed till 30% strain with a deformation rate of 2 mm/min. The data were corrected for machine compliance according to the 'direct technique' [19]. The stress-strain curves were then used to determine the mechanical properties in accordance with ISO 13314:2011 [20]. The elastic modulus, or *quasi-elastic gradient* according to the ISO standard, was calculated at the beginning of the linear region. The yield strength (σ_y), or *compressive offset stress*, was measured at 0.2% plastic compressive strain.

Two specimens of each design were subjected to a compression-compression fatigue test (MTS, Eden-Prairie, USA) (Fig. 1). The low-density specimens (RD $\approx$ 5%, $\approx$ 25%) were subjected to a maximum applied stress of 0.5 σ_y using a loading ratio (R) of 0.1 and a frequency of 15 Hz. Due to the extraordinary fatigue life of the high-density specimens (RD $\approx$ 45%) [12], these specimens were subjected to a maximum applied stress of 0.7 σ_y using the abovementioned loading ratio and frequency. To visualize the deformation and crack propagation over time, the fatigue tests were stopped at 25% (specimen #1) and 50% (specimen #2) of the maximum number of cycles found in [12].

2.4.1. Digital image correlation

The exterior strains and displacements were measured using the digital image correlation (DIC) technique by comparing im-

ages of the specimens at different stages of deformation [21]. To create sufficient image texture, a random and unique speckle pattern had to be applied to the surface of the specimen. The whole specimen was, therefore, spray-painted in black, while its frontal surface was manually painted in white. A black speckle pattern was eventually added using an airbrush [3,11]. During fatigue testing, two 4 Megapixel digital cameras (Limess, Krefeld, Germany) were used to capture the frontal surface of the specimens under maximum load (Fig. 1). This was done at a regular interval with a total of 100 images for specimen #1 and 150 images for specimen #2. The DIC system was calibrated using the Vic-Snap software (Correlated Solutions Inc., Irmo, USA) and the images were analyzed using Vic-3D 8 (Correlated Solutions Inc., Irmo, USA). The major principal strain (*e1*) was calculated for all the specimens.

2.5. Micro computed tomography

X-ray micro computed tomography (micro-CT) is a non-destructive imaging technique growing in popularity for materials science and engineering applications [22]. It is increasingly used in the field of additive manufacturing to qualitatively or quantitatively evaluate manufactured parts, as reviewed in [23]. In this work, micro-CT was used to evaluate the occurrence and location of fatigue cracks/fractures in the additively manufactured auxetic meta-biomaterials that were previously subjected to fatigue testing (Fig. 1).

Micro-CT scans were acquired with a GE Phoenix Vtomex L240 system (GE, Boston, USA), using 200 kV and 100 µA for X-ray generation and with 0.5 mm copper beam filtration. The images were acquired in 3200 steps during a full rotation of the sample, using 333 ms acquisition time for each image. The system uses a stepwise rotation, with the first image at each step being discarded to build in some stabilization time and improve the quality of the scan. To accommodate the sample size, the voxel size was set to 30 µm for a full-scale lattice evaluation. These scans were reconstructed using the system supplied Datos software and image analysis and evaluation were performed in Volume Graphics VGSTUDIO MAX 3.4 (Volume Graphics GmbH, Heidelberg, Germany). A de-noising filter (adaptive Gauss default) was applied followed by the manual alignment of the sample in the three orthogonal cross-sectional viewing planes (the sample was scanned at an angle to improve the image quality and minimize image artifacts). An additional step of manual inspection was performed in search of cracks and fractures for which the contrast was further optimized. Cross-sectional greyscale images were made at selected locations. Based on the manual inspection, a classification was made to define the extent of fatigue damage that was observed in each specimen.

Table 1

The nominal (*i.e.*, designed) and actual dimensions of the specimens (types A-D). The values are presented as mean ± standard deviation.

Type	RD [%]	Diameter [mm]		Height [mm]	
	CAD	CAD	As-manufactured	CAD	As-manufactured
A	4.6	24.99	25.34 ± 0.09	35.92	35.85 ± 0.04
	24.1	25.50	25.70 ± 0.11	36.44	36.34 ± 0.05
	42.7	25.86	25.87 ± 0.17	36.79	35.46 ± 0.45
B	5.4	24.51	24.92 ± 0.06	36.22	36.12 ± 0.02
	25.4	24.99	25.23 ± 0.10	36.69	36.55 ± 0.05
	45.4	25.32	25.58 ± 0.08	37.02	35.20 ± 0.61
C	4.9	22.20	22.56 ± 0.04	35.58	35.49 ± 0.01
	24.6	22.57	22.79 ± 0.09	35.95	35.77 ± 0.02
	43.2	22.83	23.10 ± 0.11	36.21	35.36 ± 0.41
D	3.4	22.00	22.39 ± 0.06	35.57	35.51 ± 0.03
	17.5	22.34	22.58 ± 0.09	35.91	35.76 ± 0.03
	32.5	22.58	22.79 ± 0.06	36.15	34.25 ± 0.88

3. Results

3.1. Morphological characteristics

The AM specimens generally matched their intended designs, save for the limited warping observed in the high-density specimens. Comparing the actual dimensions (Table 1) of the specimens with their designs showed that the diameter of the as-manufactured parts was generally bigger than the designed value while the height was smaller. The relative density values measured using the dry-weighing technique ranged between 6.3% and 43.8% (Table 2). In most cases, the relative density values were higher than the design values, except for the high-density designs (RD ≈ 45%).

3.2. Finite element modeling

The three-dimensional FE models showed that the location of stress concentrations was similar for all designs, independent of their aspect ratio and re-entrant angle (Fig. 2). The vertical struts mainly experienced compressive stresses, while the inverted struts experienced tensile stresses. The vertical struts located along the outer rim of the specimen, experienced compressive stress on the inside and tensile stress on the outside. This was primarily observed in the high-density designs. The highest stresses were found in the inverted nodes, as well as in the vertical struts located along the outer rim of the specimens. The highest tensile stresses were found at the center of the bow-tie geometry (depicted in orange/red), where all inverted struts meet (Fig. 2A). The highest compressive stresses were generally found on the other side of this node (depicted in cyan blue), where the four inverted struts are connected to a fifth vertical strut (Fig. 2A). The differences between the maximum stress values corresponding to the different designs were relatively small, but the maximum principal stress was found to increase with the aspect ratio and decrease with re-entrant angle (Fig. 2B). The differences between A and B were negligible, while the differences between C and D were more substantial, especially for the compressive stress components.

3.3. Quasi-static and fatigue performance

From previous research, we know that the deformation behavior of this type of auxetic meta-biomaterial does not always follow the typical stress-strain curve of most porous biomaterials [11,12]. The low-density specimens exhibited a typical linear region followed by a high number of fluctuations. The number of fluctuations decreased with the relative density, until they finally disappeared in the high-density specimens (RD ≈ 45%), except for de-

sign D. A first local maximum was, therefore, absent in the stress-strain curves of designs A, B and C, and the stress kept on increasing with strain.

All the designs showed an increase in their mechanical properties with the relative density (Table 2). Both stiffness and strength were found to increase with the aspect ratio and decrease with the re-entrant angle. However, the differences between designs A and B were very small. The elastic moduli ranged between 66.47 ± 1.23 MPa and 6899.45 ± 2141 MPa for the aforementioned range of the relative density. The yield strength values were found to vary between 1.43 ± 0.02 MPa and 52.09 ± 2.36 MPa for the same range of the relative density.

The compression-compression fatigue tests were performed up until 25% and 50% of the total number of cycles to failure reported in our previous study [12] (Table 2). The initial plan was to observe the specimens up until 75% of the total number of cycles to failure, but this testing protocol was changed once a few specimens failed prematurely. The specimens that were subjected to this initial protocol have been labeled with an asterisk (*). The strain *vs.* cycles graphs have been presented in Fig. 3, mainly showing the second stage of the typical three-stage strain behavior of porous metals [24]. The first stage has been cut off for convenience. The curves have been presented till 50% of the cycles to failure, also for the specimens tested till 75%. In most cases, the strain *vs.* cycles graph showed that there is hardly any buildup of strain, but some of the specimens failed before reaching 50% of their cycles to failure. The specimen #2 of design A (RD = 42%) reached stage III and showed a diagonal failure profile (Fig. 3A). Two of the specimens of design B (RD = 28% and RD = 44%) exhibited a gradual increase in strain, but no failure could be observed yet (Fig. 3B). A similar observation was made for the specimen #2 of design C with a relative density of 26% (Fig. 3C). The onset of stage III was also observed in the strain *vs.* cycles graph of design D (specimen #1 and #2 with RD = 32%). Failure was observed in the specimen #2 of design D with a relative density of 19%, showing the complete collapse of one horizontal layer, matching the rapidly accumulating strain in the graph (Fig. 3D).

3.4. External signs of fatigue failure

The external strain development was assessed with the help of DIC to look for strain concentrations and possible crack initiation sites. Some specimen results have been presented in Fig. 4. Principal strain concentrations were mainly found in the inverted nodes and in the vertical struts located along the outer rim of the specimens (Fig. 4A) especially in the high-density specimens (RD ≈ 45%). In the latter, clear differences were observed between the lateral and medial sides of these vertical struts (Fig. 4B). The lateral side generally exhibited positive strain (tension), whereas the medial side exhibited negative strain (compression). In the high-density specimens of designs A and B, local strain concentrations were found in the DIC paint connecting the inverted struts. The low-density specimens exhibited little to no strain differences and limited strain concentrations throughout their structure. The area of concentrated strain developed throughout the fatigue test, growing in size (area) and magnitude (Fig. 4C). Ultimately, this led to the premature failure of some specimens. In others, design C (RD = 26%) and design D (RD = 19%), the strain distribution did not predict the location of ultimate failure.

3.5. Internal signs of fatigue failure

The internal morphology, visualized with the help of micro-CT imaging, was used to classify the specimens as follows: (I) no signs of failure, (II) micro damage and crack initiation sites, and

Table 2

The nominal (*i.e.*, designed) and actual values of the relative density of the auxetic meta-biomaterials accompanied by their *quasi-static* mechanical properties and number of cycles to failure. The values are presented as mean ± standard deviation.

| Type	RD [%]		Elastic modulus [MPa]	Yield strength [MPa]	Cycles to failure
	CAD	Dry weighing	Compression test	Compression test	Fatigue test [12]
A	4.6	7.02 ± 0.02	71.64 ± 0.45	1.44 ± 0.02	420,685
	24.1	25.79 ± 0.23	946.59 ± 49.15	16.37 ± 0.40	387,165
	42.7	41.87 ± 0.90	3231.30 ± 639.2	32.87 ± 6.50	254,569
B	5.4	8.46 ± 0.14	66.47 ± 1.23	1.43 ± 0.02	444,844
	25.4	27.68 ± 0.33	1171.79 ± 21.20	16.99 ± 0.51	395,336
	45.4	43.78 ± 1.37	3353.88 ± 201.7	34.37 ± 1.38	261,861
C	4.9	9.32 ± 0.15	224.06 ± 10.91	3.74 ± 0.09	149,477
	24.6	25.97 ± 0.13	1992.62 ± 83.20	26.93 ± 0.43	464,868
	43.2	41.70 ± 0.35	6899.45 ± 2141	52.09 ± 2.36	943,220
D	3.4	6.25 ± 0.04	118.84 ± 0.93	1.80 ± 0.01	175,580
	17.5	18.96 ± 0.14	1303.78 ± 20.83	15.69 ± 0.38	346,327
	32.5	31.60 ± 0.15	3756.24 ± 357.7	31.94 ± 1.55	546,674
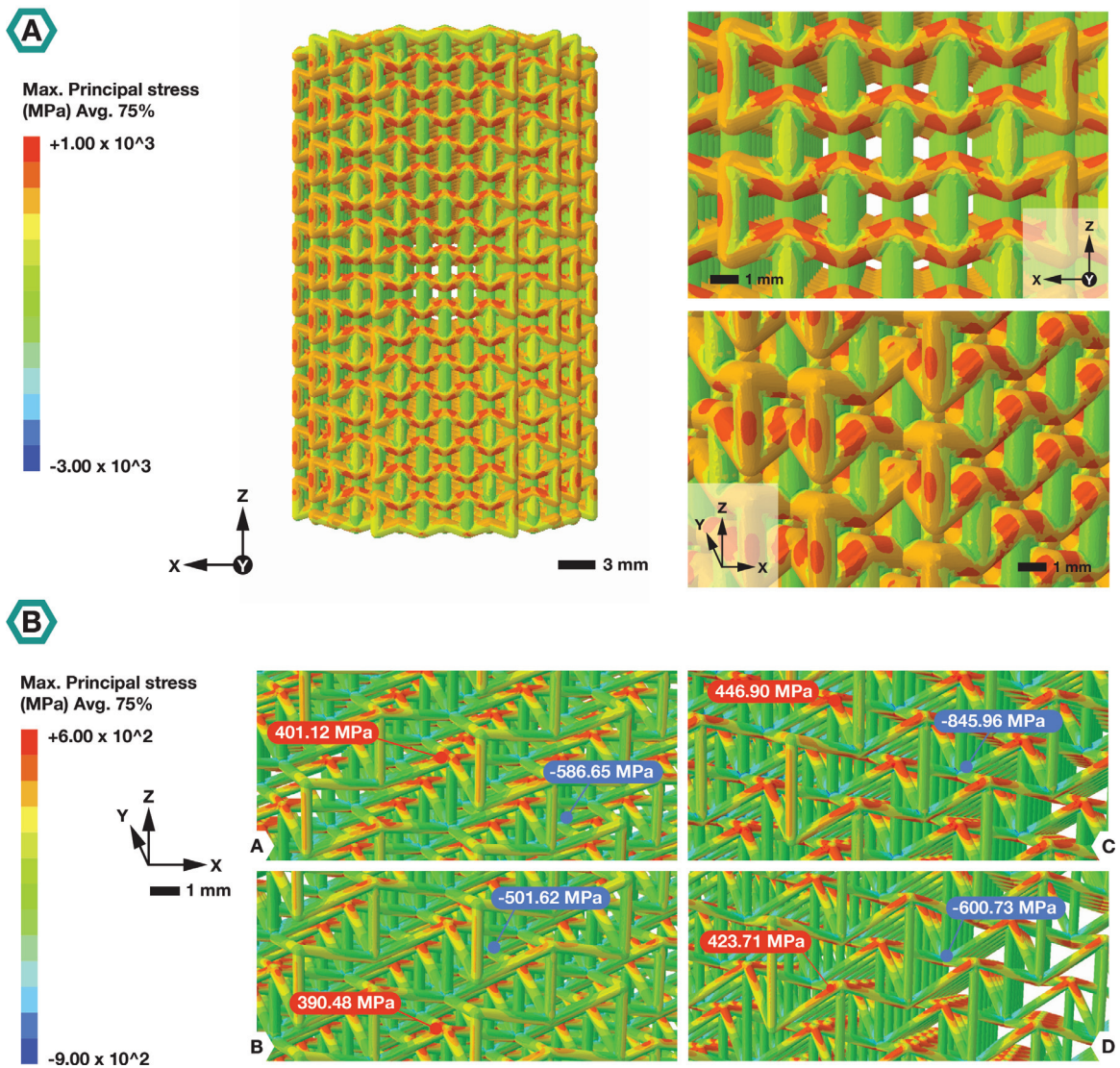
Fig. 2. (A) Finite element model of design C (RD = 42%), showing the stress concentrations in the structure under compressive loading. (B) Finite element models of designs A-D (RD = ≈ 5%) showing the differences in the mean absolute maximum principal stresses.
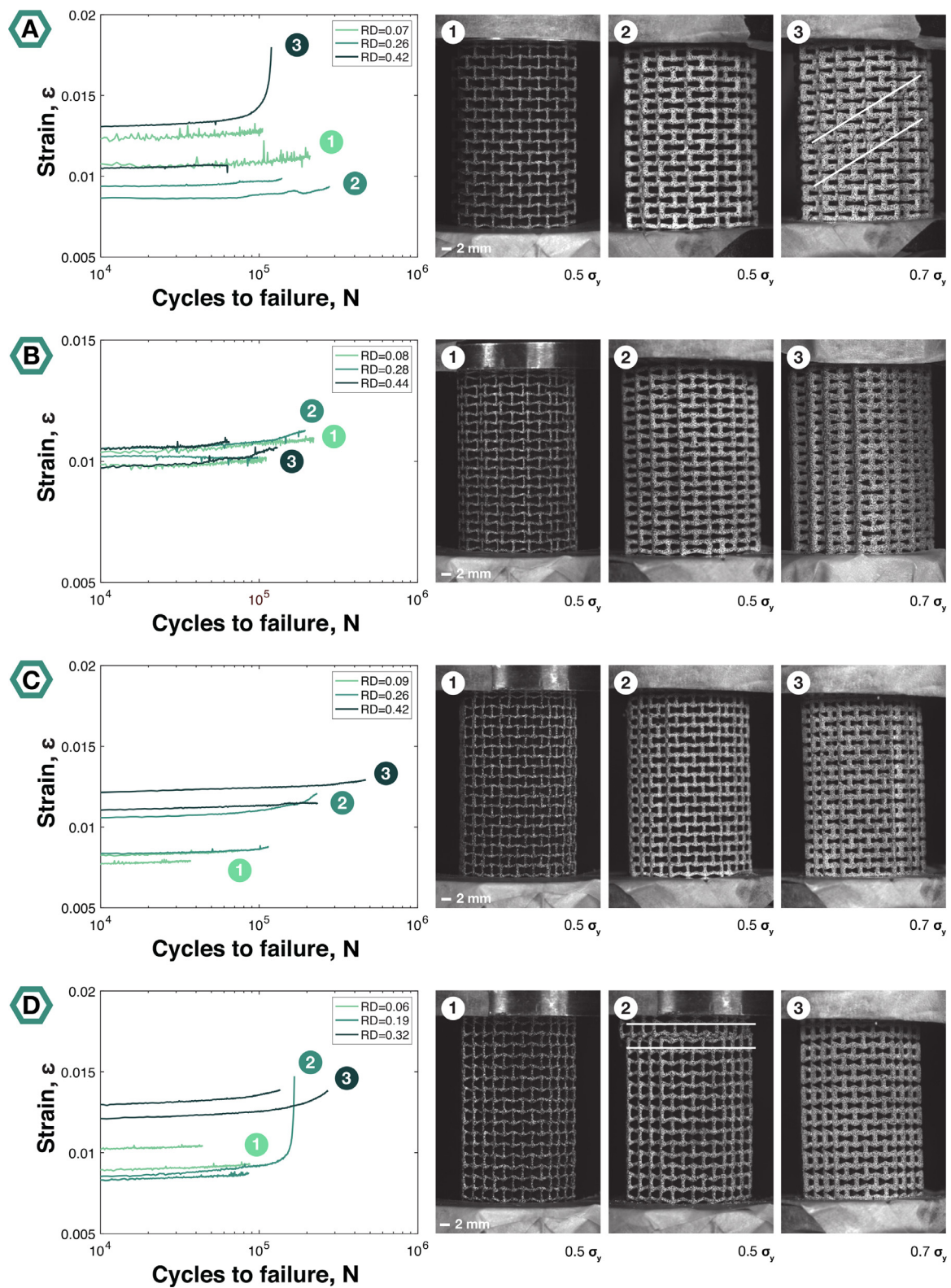
Fig. 3. (A) Strain *vs.* cycles curves of all type A specimens tested, including the appearances of specimen #2 with (1) RD = 7%, (2) RD = 26%, and (3) RD = 42%. (B) Strain *vs.* cycles curves of all type B specimens tested, including the appearances of specimen #2 with (1) RD = 8%, (2) RD = 28%, and (3) RD = 44%. (C) Strain *vs.* cycles curves of all type C specimens tested, including the appearances of specimen #2 with (1) RD = 9%, (2) RD = 26%, and (3) RD = 42%. (D) Strain *vs.* cycles curves of all type D specimens tested, including the appearances of specimen #2 with (1) RD = 6%, (2) RD = 19%, and (3) RD = 32%.
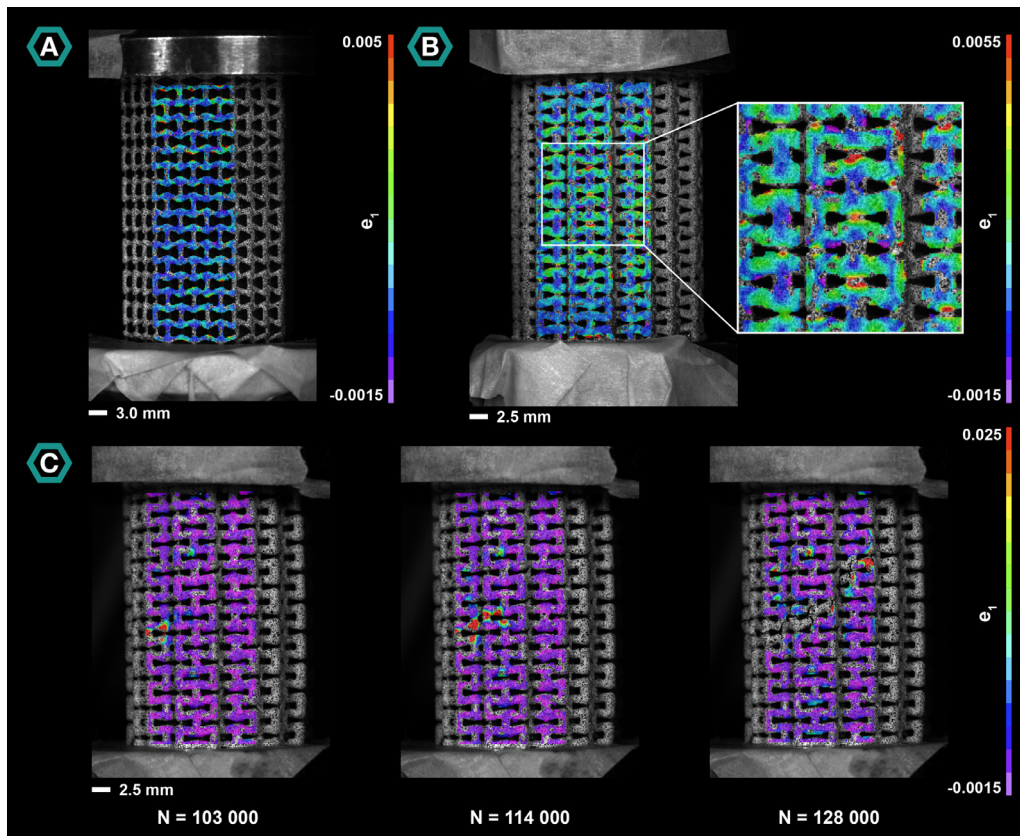
Fig. 4. (A) Major principal strain distribution in design D (RD = 19%, specimen #1) under the maximum load. (B) Local strain variations through the thickness of the struts in design B (RD = 44%, specimen #1). (C) Strain development in design A (RD = 42%, specimen #2) right before and shortly after fatigue failure.

(III) substantial crack growth/fractures. The results of this classification have been presented in Fig. 5, showing an increase in the fatigue damage with the number of fatigue cycles. All the low-density specimens (RD ≈ 5%) were still intact, even after being exposed to 50% of their cycles to failure, showing a homogeneous deformation. In the second group (RD ≈ 25%) most specimens exhibited early signs of fatigue failure, with crack initiation in the first phase (#1), followed by substantial crack growth in the next (#2). Crack initiation was primarily observed in the nodes (mode-I), or in the middle of the vertical struts. The specimens eventually failed at the same locations, with fractures perpendicular to the strut length. Design A (RD = 26%, #2) and design C (RD = 26%, #1) both exhibited a line of destruction along the outer rim of the specimen, whereas a full layer collapsed in the top half of design C (RD = 26%, #2) and design D (RD = 19%, #2). The latter mainly exhibited fractures in the failed layer, or close surroundings, the rest of the structure remained intact. Some of the high-density specimens (RD ≈ 45%) made it through 50% of the cycles without signs of failure, while others exhibited substantial cracking at 25%. Many of the microcracks were found to originate from the internal voids, which were quite substantial in the high-density specimens. A diagonal failure profile could be observed in design A (RD = 42%, #2), in which all the failed unit cells fractured in the middle of the inverted nodes (mode-I, Fig. 6A). The specimens of design C (RD = 42%) exhibited fractures in the vertical struts. Fatigue failure was observed around the inverted nodes of design D (RD = 32%, #2), while specimen #1 exhibited one through fracture in a vertical strut. All the above-described fractures for designs C and D were located along the outer rim of the specimens.

4. Discussion

We additively manufactured four different types of auxetic meta-biomaterials, each of which with three different values of the relative density, and subjected them to cyclic loading. In a previous study [12], we had primarily looked at the S-N curves of the same designs. Here, we focused on the mechanisms of crack initiation and propagation over time. External strain measurements were made using DIC, and the internal structure was evaluated with the help of micro-CT at different stages of the fatigue cycle. The results of this study contribute to the full understanding of the fatigue performance of AM auxetic meta-biomaterials.

4.1. Crack initiation and propagation in (AM) metals

Fatigue cracks are often initiated at geometrical discontinuities (*e.g.*, holes and notches) or microstructural irregularities (*e.g.,* voids, cavities and non-metallic inclusions) that function as macro- or microscopic stress raisers [25]. In the absence of these defects, strain concentrations may develop due to the irreversible dislocation motion of the material's crystallographic structure (microplasticity). In AM materials, dislocations primarily arise because of plastic strain due to thermal expansion or shrinkage [26]. Under continued cyclic loading unique structures are formed in an attempt to minimize the system's total energy (persistent slip bands (PSBs)), which eventually lead to the formation of cracks within the crystal grains [27,28]. On the surface, a pronounced surface relief may arise, also known as persistent slip markings (PSMs). Physical models have been proposed to predict the extrusions and intrusions preceding the formation of PSBs and PSMs [29,30]. In
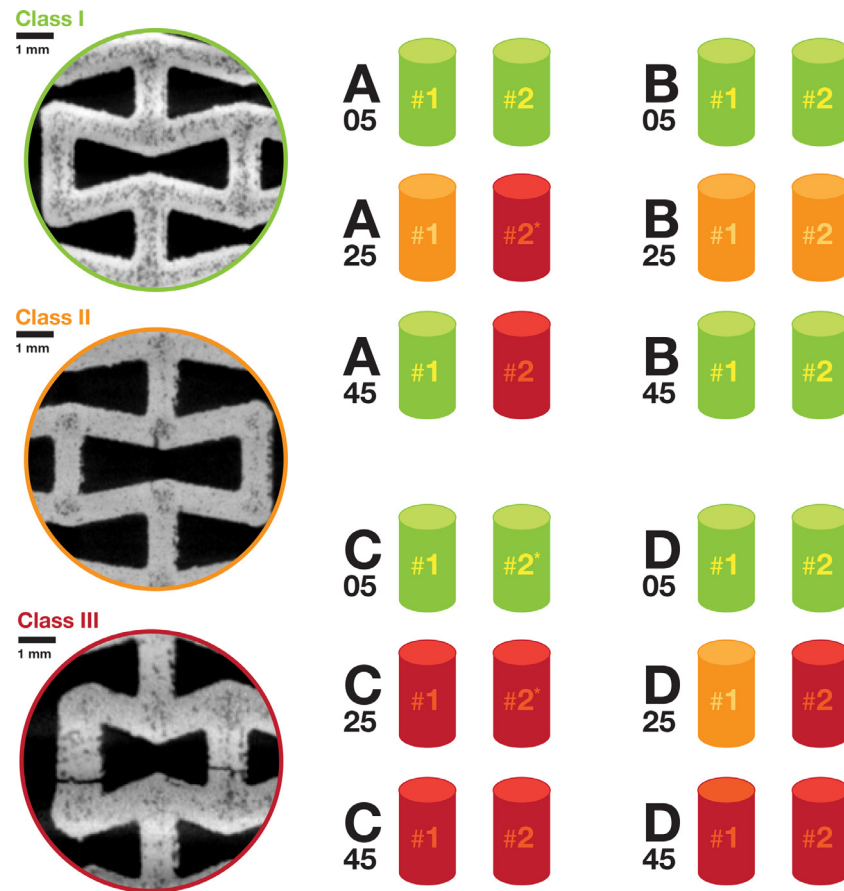
Fig. 5. Classification of the specimens after manual inspection of their micro-CT data. Class I specimens exhibited no signs of fatigue failure, Class II specimens exhibited micro-damage and crack initiation sites, Class III specimens showed substantial crack growth. Specimens labelled with an * were tested till 75% of the cycles to failure.

general, Polàk's model was found to be in good agreement with experimental data, effectively modeling the growth of extrusions and the delayed emergence of intrusions, and hence the process of crack initiation [30,31]. Cracks may also grow from grain boundaries as a result of slip impingement, but are far more common to nucleate in defects such as the ones mentioned above [28]. In the stages leading up to component failure, the cracks will propagate through neighboring grains. Cracks that are nucleated in defects often grow in the direction perpendicular to the applied loading direction [15].

Defects may be the result of the manufacturing process, and while the incidence of these defects in traditionally fabricated parts is relatively small, they are still dominant in AM materials [32–34]. Such defects would include, among others, spherical pores as a result of gas entrapment, irregular lack of fusion (LoF) voids (generally the most detrimental) and a rough surface due to the layer-by-layer build-up [32,35,36]. Strut-based lattices are generally more susceptible to these defects, given their effective size compared to the strut diameter. The thermal history of the printed part also strongly affects the microstructure, the residual stresses and the incidence of defects, and may result in inter- and intra-batch variations [32,33,36]. The structure and density of dislocations can be controlled through the manipulation of processing parameters [26]. The cooling rate could for instance be tuned to alter the spacing of dendrite arms, which generally hinder dislocation motion. Furthermore, the location of residual stresses is determined by the thermal gradient, while the magnitude of accumulated strain is guided by the hatch and layer spacing [26]. Porous structures, like the ones presented here, generally fail as a result of mode-I crack initiation and propagation in the struts. Similar to

the *quasi-static* collapse of individual struts, fatigue cracks will also choose the weakest path [37,38]. In the following paragraphs we will take a closer look at the data, considering the important roles of printing quality and manufacturing defects in determining the fatigue behavior of auxetic meta-biomaterials.

4.2. Quasi-static and fatigue performance

The auxetic meta-biomaterials did not always exhibit the typical deformation behavior found in previous studies on porous bio-materials [11,39]. While low-density specimens did show a linear region followed by high frequency fluctuations, these fluctuations disappeared as the relative density increased. The geometry of the unit cells in combination with a high relative density causes the cell walls to touch at a lower value of the applied strain. As a result, the structures go through early densification, and the stress continues to increase with strain [40]. In such cases, there are no local maxima, and the structures start to behave like solids. Ultimately, these structures will fail too, but at higher values of strain. The stress-strain curves that were obtained here, match the deformation behavior of the geometrically identical specimens in our previous study [12]. The mechanical properties followed the same geometry-property relationships [7,11,12], but the absolute values slightly differed. In general, the specimens in this study exhibited a higher elastic modulus and yield strength. In most cases, these differences were not significant, but a substantial increase was found for designs B and C (RD ≈ 45%). These deviations can be attributed to the complexity of the unit cell geometries, which pushed the boundaries of the AM process and caused a high degree of inter-specimen variability [41–43]. This was also confirmed by the rela-
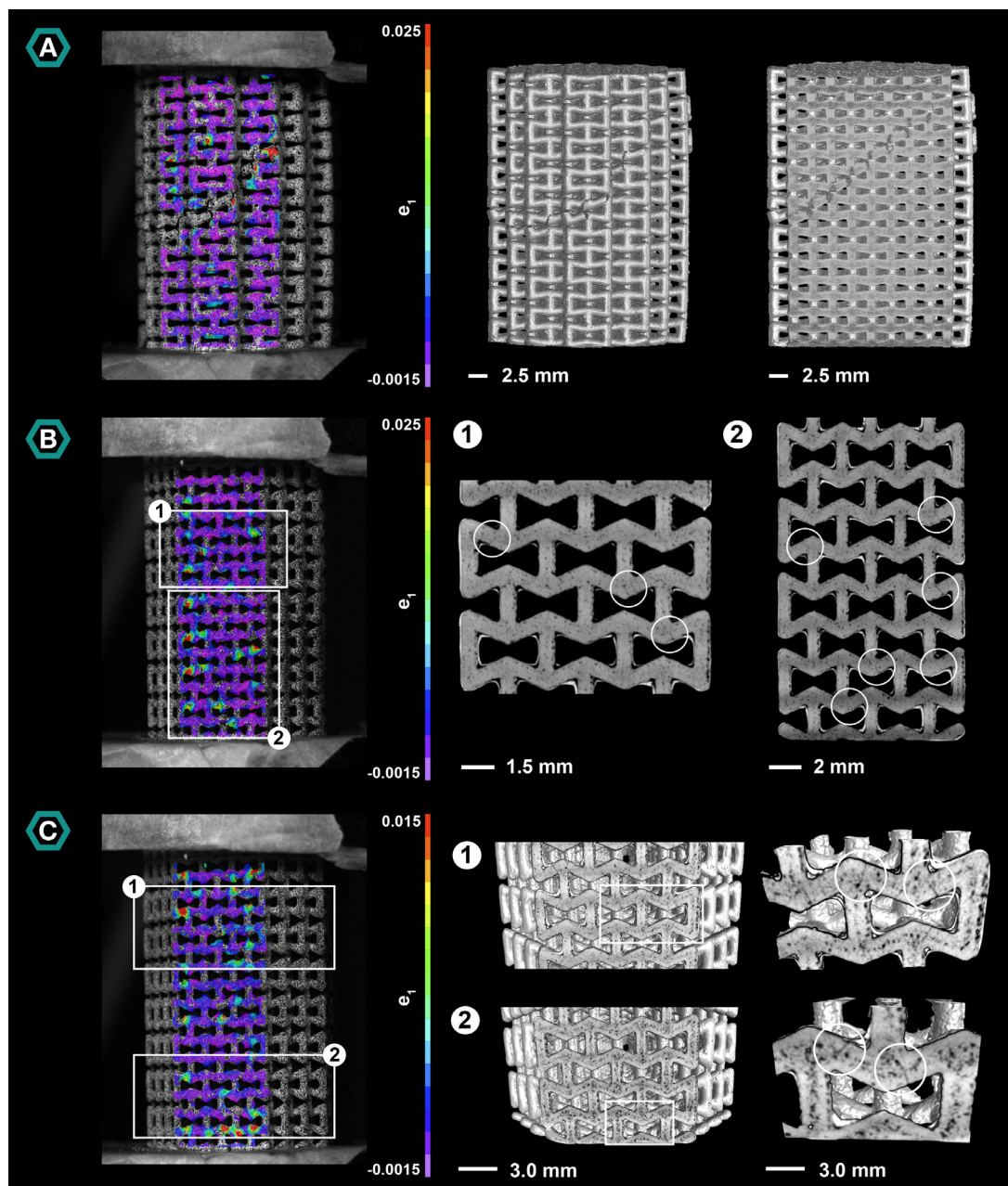
Fig. 6. The correlation between the DIC strain profiles and micro-CT images of (A) Design A (RD = 42%, specimen #2), (B) Design D (RD = 32%, specimen #1), (C) Design D (RD = 32%, specimen #2).

tively high standard deviations found for design C, both here and in the previous study [12]. Additionally, there are always some unavoidable inter-batch differences caused by the variations in the processing parameters (*e.g.*, powder particle size and laser power) [44].

The specimens were subjected to compression-compression fatigue testing, with the intention to stop the test before reaching stage III (rapid strain accumulation and specimen failure) [24]. According to the strain *vs.* cycles graphs, we managed to achieve that for most of the specimens. However, two of the specimens exhibited a rapid increase in their strain and failure was confirmed by the collapse of at least one layer of their unit cells. The premature failure of these specimens, before reaching 50% of the maximum number of cycles reported in (Table 2) [12], may be attributed to the inter-specimen variability. Slight differences in their micro-architecture and the presence of poten-

tial crack nucleation sites may have decreased their fatigue lives [45,46].

Even slight increases in the strain, which can be considered as the onset of stage III or a potential strain jump [24], were found to coincide with micro-cracks and crack initiation sites in the micro-CT images. In some cases, substantial crack growth was observed in the specimens with a nearly flat strain *vs.* cycles curve (*e.g.*, design C, RD = 42%) (Fig. 3C). This can be explained by the location of these fractures, which were all located in the vertical struts, perpendicular to the loading direction.

Despite the compressive loading, not all the vertical struts were under full compression (Fig. 2). The FE element models confirmed that high tensile stresses are present in the vertical struts located along the outer rim of the specimens, since they are forced to bend in response to the rotation of the inverted struts. Tensile and compressive stresses and strains were, therefore, observed through the

thickness of the struts in both FE models and DIC strain profiles of the high-density specimens. This makes them more susceptible to failure as compared to the vertical struts located on the inside of the specimens. The structures remained intact under compressive loading if the fractures were solely present in the vertical struts. This loading profile causes crack closure and will therefore slow down crack growth, whereas tensile loading generally enhances crack propagation [47–49]. Furthermore, the relatively thick strut junctions in the high-density specimens limit the rotation of the struts and may, therefore, increase the compressive loading component [12]. This may further extend the fatigue life when simply looking at the strain *vs.* cycles graphs.

4.3. External *vs.* internal signs of fatigue failure

The principal strain profiles closely matched the maximum principal stress locations found in the FE models. The inverted nodes and vertical struts located along the outer rim of the specimens may, therefore, be considered as the "weak spots". This was once more confirmed by the micro-CT data in which cracks were mainly found around these locations. With high tensile stresses in the inverted nodes, the mode-I cracks formed around this weak spot were generally more deleterious to the structural integrity. Similar results were found in other studies, probably as a result of stress concentrations due to the overlapping strut volume and their susceptibility to geometrical imperfections [15]. According to the FE models, designs C and D are the most susceptible to mode-I cracking, although the differences are relatively small. It should also be noted that the magnitude of the maximum principal stress in design C can be the result of the chosen meshing strategy.

Cracks were not always observed near the DIC surface, but in some cases a perfect match was found between the DIC strain profile and the micro-CT images (Fig. 6). The diagonal shear profile in design A (RD = 42%) was, for instance, found to extend all the way through the thickness of the structure (Fig. 6A). The high strain locations in design D (RD = 32%) perfectly matched the fractures found in the micro-CT images. Fractures were generally found in high strain areas (red), whereas crack initiation was apparent in medium strain areas (green) (Fig. 6B). The high-density specimens were also found to exhibit a relatively high micro-porosity, which could strongly affect their fatigue performance [35,50]. Indeed, cracks were found to originate in these irregular void spaces especially around the weak spots (Fig. 6C). Simple design changes, such as the application of fillets in corners, could limit the stress concentrations near these weak spots [15]. Further optimizing the scanning parameters as well as the application of post-manufacturing processes, such as hot isostatic pressing (HIP) [50–52], could contribute to a more solid build by minimizing the lack of fusion voids. Additionally, it would relax the residual stresses and improve the ductility of the material, but it often does not affect the failure mechanism [33]. Crack nucleation sites on the surface or sub-surface, as a result of the high surface roughness, primarily control the cracking behavior [28,53]. These could potentially be eliminated by chemical or (thermo)mechanical surface treatments [46,52,54,55].

Inspecting the location of the fatigue damage in each of the designs revealed clear differences that are expected to have originated from the geometry of the underlying unit cells. This is expected given the compression-compression nature of the reported fatigue experiments and the fact that the macroscale compressive stresses translate to different levels of tensile stresses at the strut level, depending on the type of unit cell. Such differences eventually lead to different fatigue behaviors. For example, the unit cell layers of designs A and B were found to deform and fail completely under compressive loading [12]. This was once more confirmed by the micro-CT data, showing crack initiation and growth throughout

the layers of the structures. In designs C and D, the observed cracks were clustered, especially in the designs with a relative density of ≈ 25%. This resulted in the full collapse of one of the top layers, while the rest of the structure remained intact [12]. With the absence of DIC strain concentrations, the failure of these layers came relatively unexpected. The location of failure could, however, be explained, since the load was applied at the top and had to be transferred through fairly thin struts. The upper half will therefore experience permanent plastic deformations, prior to the bottom half. Short of performing ultrahigh frequency imaging, the time difference between consecutive images taken during DIC measurements is too large to allow for capturing the strain distribution associated with the incident of failure.

According to the strain distributions and micro-CT images, there are several cases in which the specimen "failed" (Class III), although their strain *vs.* cycles graph indicated otherwise. These observations suggest that the structures maintained their integrity even though some of their struts fractured. While this may not be a problem for some applications, it is not acceptable for meta-biomaterials where patient safety is paramount. Upon strut failure, the structure may release metal powder particles that can travel through the body, eliciting the foreign body response of the patient's immune system. As a direct consequence of the activated signaling pathways, bone resorption will take place and the implant-bone interface will lose its integrity [9,10]. The potential impact of this particle debris should be studied *in vivo*, since the severity of the situation also depends on the size of the particles and the rate at which they accumulate [9]. The extraordinary fatigue lives of the high-density specimens of designs C and D should, therefore, be re-evaluated, by taking a closer look at their microstructure [12]. That is particularly true given the fact that even #1 specimens exhibited substantial crack growth. Eventually, bone ingrowth will increase the fatigue performance of the bone-implant complex and potentially eliminate the weak spots, but till then the structures should maintain their structural integrity [56].

Surprisingly, the low-density designs (RD ≈ 5%) made it through the fatigue tests without any signs of failure. This was confirmed by the DIC data, micro-CT images, and strain *vs.* cycles graphs. As compared to the high-density designs (RD ≈ 25% & ≈ 45%) that have thicker struts, the contribution of the bending stresses to the deformation of the struts of these designs is relatively limited. This was confirmed by the different stress distributions through the thickness of the vertical struts (Fig. 2 & 4B). The signs of mode-I crack initiation and propagation were, therefore, more clearly visible in the micro-CT images of the high-density designs as compared to the low-density specimens. Based on these observations, low-density specimens seem to generally have a higher fatigue life than high-density specimens when subjected to the same normalized loading profile [38]. This was not necessarily confirmed by the normalized S-N curves in the previous study [12], but this may change once the microstructure of the specimens is further examined. Additionally, hardly any microporosity was found in the low-density specimens [12], which limits the number of crack nucleation sites and may therefore increase their fatigue performance.

4.4. Future research

The results of this study suggest that the fatigue performance of auxetic meta-biomaterials should be studied at both the macroscale using strain *vs.* cycles graphs and S-N curves and at the microscale using microarchitectural characterization techniques. Future research into the fatigue behavior of architected materials in general and auxetic meta-biomaterials in particular should, therefore, combine the methods used in this paper with the compression-compression fatigue protocol used in our previ-

ous study. Such types of studies would require a large number of specimens. The use of ultrafast imaging techniques with imaging frequencies ≫ 1 Hz would also make it possible to capture the event of failure in greater detail.

Compression is considered the most dominant loading type in the musculoskeletal system, which explains the high number of fatigue studies that have used this loading mode [14,47,48,57-59]. It is, however, important to not only study the effects of other loading regimes (*e.g.*, tension-tension and compression-tension), but also consider the impact of mixed-mode loading scenarios. For example, in the hip stem designs proposed before where the auxetic meta-biomaterials primarily experience tension due to bending [3]. The results of this study show that tension could increase the rate of crack formation in the vertical struts, compromising the structural integrity of the specimens and decreasing the maximum number of cycles to failure. The fatigue performance of these auxetic meta-biomaterials should, therefore, be studied under all applicable loading conditions. This will require some adjustments in the specimen's geometry (*e.g.*, incorporation of functional gradients), to facilitate the tensile load transfer from the machine to the sample [15]. These aspects could also be considered as a way to investigate the effects of the anisotropic properties of AM materials, which may have been caused by the geometry of the unit cells or the AM process itself, on the fatigue behavior of meta-biomaterials. Furthermore, the biological effects of the released particle debris as well as the effects of the biological environment on the fatigue lives of implants should be studied.

5. Conclusions

In this study, the mechanisms underlying crack initiation and propagation in twelve different types of AM auxetic meta-biomaterials subjected to compression-compression fatigue testing were studied. Geometrical variations in the re-entrant hexagonal honeycomb resulted in four different designs (A-D), while each of them was manufactured in three different relative density classes (RD ≈ 5%, ≈ 25%, ≈ 45%). FE models were made to study the location of weak spots inside the structure, while their *quasi-static* mechanical properties were acquired in a compression test. Two specimens of each design were subjected to a compression-compression fatigue test, running till 25% or 50% of the maximum number of cycles. DIC images were made simultaneously to evaluate the evolution of the strain distribution with cyclic loading. Once the fatigue tests were stopped, the micro-architecture of the specimens was evaluated with the help of micro-CT imaging. Weak spots were identified in the FE models and generally matched the maximum principal strain concentrations and accompanying fracture sites in the DIC and micro-CT data. Many of the cracks were found to originate in the internal void spaces or at locations susceptible to mode-I cracking. The differences between the different designs were relatively small and could only be observed when looking at the location of the fatigue damage. Most of the specimens maintained their structural integrity (according to their strain *vs.* cycles graph) despite the presence of substantial crack growth. This may result in the release of powder particles that could elicit the foreign body response of the patient's immune system, and thereby jeopardize the implant's success. These observations indicate that finding the right failure criterion for auxetic meta-biomaterials is quite challenging. Future research should, therefore, always include a micro-architectural assessment to check for the damage accumulated in the structures even in the absence of rapid strain accumulation. This also highlights the importance of studying other loading regimes, as cracks generally grow much faster under tension, especially the mode-I cracks found in the auxetic meta-biomaterials studied here. Both the design and the processing parameters could be optimized to limit the number of

weak spots and potentially improve the fatigue performance of the auxetic meta-biomaterials.

Disclosures

None.

Declaration Of Competing Interest

The authors declare that they have no known competing financial interests or personal relationships that could have appeared to influence the work reported in this paper.

Acknowledgements

References

[1] A.A. Zadpoor, Mechanical meta-materials, Mater. Horiz. 3 (5) (2016) 371–381.
[2] F. Bobbert, K. Lietaert, A.A. Eftekhari, B. Pouran, S. Ahmadi, H. Weinans, A. Zadpoor, Additively manufactured metallic porous biomaterials based on minimal surfaces: a unique combination of topological, mechanical, and mass transport properties, Acta Biomater. 53 (2017) 572–584.
[3] H.M. Kolken, S. Janbaz, S.M. Leeflang, K. Lietaert, H.H. Weinans, A.A. Zadpoor, Rationally designed meta-implants: a combination of auxetic and conventional meta-biomaterials, Mater Horiz 5 (1) (2018) 28–35.
[4] A.E.H. Love, A treatise on the mathematical theory of elasticity, Cambridge university press, 2013.
[5] Y. Prawoto, Seeing auxetic materials from the mechanics point of view: a structural review on the negative poisson's ratio, Comput. Mater. Sci. 58 (2012) 140–153.
[6] A. Alderson, A triumph of lateral thought, Chem. Ind. 17 (1999) 384–391.
[7] H.M. Kolken, A. Zadpoor, Auxetic mechanical metamaterials, RSC Adv. 7 (9) (2017) 5111–5129.
[8] J. Wolff, Das gesetz der transformation der knochen, A Hirshwald 1 (1892) 1–152.
[9] Y. Abu-Amer, I. Darwech, J.C. Clohisy, Aseptic loosening of total joint replacements: mechanisms underlying osteolysis and potential therapies, Arthritis Res. Ther. 9 (1) (2007) 1–7.
[10] M. Sundfeldt, L.V. Carlsson, C.B. Johansson, P. Thomsen, C. Gretzer, Aseptic loosening, not only a question of wear: a review of different theories, Acta Orthop 77 (2) (2006) 177–197.
[11] H. Kolken, K. Lietaert, T. van der Sloten, B. Pouran, A. Meynen, G. Van Loock, H. Weinans, L. Scheys, A.A. Zadpoor, Mechanical performance of auxetic meta-biomaterials, J. Mech. Behav. Biomed. Mater. 104 (2020) 103658.
[12] H.M.A. Kolken, A.F. Garcia, A. Du Plessis, C. Rans, M.J. Mirzaali, A.A. Zadpoor, Fatigue performance of auxetic meta-biomaterials, Acta Biomater. 126 (2021) 511–523.
[13] R.O. Ritchie, Mechanisms of fatigue-crack propagation in ductile and brittle solids, Int. J. Fract. 100 (1) (1999) 55–83.
[14] R. Wauthle, S.M. Ahmadi, S.A. Yavari, M. Mulier, A.A. Zadpoor, H. Weinans, J. Van Humbeeck, J.-.P. Kruth, J. Schrooten, Revival of pure titanium for dynamically loaded porous implants using additive manufacturing, Mater. Sci. Engineering: C 54 (2015) 94–100.
[15] M. Benedetti, A. Du Plessis, R. Ritchie, M. Dallago, J. Razavi, F. Berto, Architected cellular materials: a review on their mechanical properties towards fatigue-tolerant design and fabrication, Mater. Sci. Engineering: R 144 (2021) 100606.
[16] V. Lvov, F. Senatov, A. Stepashkin, A. Veveris, M. Pavlov, A. Komissarov, Low-cycle fatigue behavior of 3D-printed metallic auxetic structure, in: Materials Today: Proceedings, 2020.
[17] J. Michalski, T. Strek, in: Fatigue Life of Auxetic *Re*-entrant Honeycomb Structure, International Scientific-Technical Conference MANUFACTURING, Springer, 2019, pp. 50–60.
[18] 3DSystems, LaserForm Ti Gr1 (A), 2017.
[19] S. Kalidindi, A. Abusafieh, E. El-Danaf, Accurate characterization of machine compliance for simple compression testing, Exp. Mech. 37 (2) (1997) 210–215.
[20] I. Standard, ISO 13314: 2011 (E) (2011) Mechanical testing of metals—ductility testing—compression test for porous and cellular metals, Ref number ISO 13314(13314) 1–7.
[21] N. McCormick, J. Lord, Digital image correlation, Mater. Today 13 (12) (2010) 52–54.
[22] P.J. Withers, C. Bouman, S. Carmignato, V. Cnudde, D. Grimaldi, C.K. Hagen, E. Maire, M. Manley, A. Du Plessis, S.R. Stock, X-ray computed tomography, Nat. Rev. Methods Primers 1 (1) (2021) 1–21.

[23] A. Du Plessis, I. Yadroitsev, I. Yadroitsava, S.G. Le Roux, X-ray microcomputed tomography in additive manufacturing: a review of the current technology and applications, 3D Printing and Additive Manufacturing 5 (3) (2018) 227–247.

[24] Y. Sugimura, A. Rabiei, A.G. Evans, A. Harte, N.A. Fleck, Compression fatigue of a cellular Al alloy, Materials Science and Engineering: A 269 (1–2) (1999) 38–48.

[25] U. Zerbst, M. Madia, C. Klinger, D. Bettge, Y. Murakami, Defects as a root cause of fatigue failure of metallic components. I: basic aspects, Eng. Fail. Anal. 97 (2019) 777–792.

[26] K. Bertsch, G.M. de Bellefon, B. Kuehl, D. Thoma, Origin of dislocation structures in an additively manufactured austenitic stainless steel 316 L, Acta Mater. 199 (2020) 19–33.

[27] M.D. Sangid, The physics of fatigue crack initiation, Int. J. Fatigue 57 (2013) 58–72.

[28] K.S. Chan, Roles of microstructure in fatigue crack initiation, Int. J. Fatigue 32 (9) (2010) 1428–1447.

[29] H. Mughrabi, Cyclic slip irreversibilities and the evolution of fatigue damage, Metallurg. Mater. Transac. B 40 (4) (2009) 431–453.

[30] J. Polak, J. Man, Experimental evidence and physical models of fatigue crack initiation, Int. J. Fatigue 91 (2016) 294–303.

[31] J. Polák, J. Man, Mechanisms of extrusion and intrusion formation in fatigued crystalline materials, Mater. Sci. Engineering: A 596 (2014) 15–24.

[32] N. Sanaei, A. Fatemi, Defects in additive manufactured metals and their effect on fatigue performance: a state-of-the-art review, Prog. Mater Sci. 117 (2021) 100724.

[33] R. Molaei, A. Fatemi, Crack paths in additive manufactured metallic materials subjected to multiaxial cyclic loads including surface roughness, HIP, and notch effects, Int. J. Fatigue 124 (2019) 558–570.

[34] R. Molaei, A. Fatemi, N. Sanaei, J. Pegues, N. Shamsaei, S. Shao, P. Li, D. Warner, N. Phan, Fatigue of additive manufactured Ti-6Al-4 V, Part II: the relationship between microstructure, material cyclic properties, and component performance, Int. J. Fatigue 132 (2020) 105363.

[35] A. du Plessis, S. Razavi, F. Berto, The effects of microporosity in struts of gyroid lattice structures produced by laser powder bed fusion, Mater. Des. 194 (2020) 108899.

[36] P. Li, D. Warner, A. Fatemi, N. Phan, Critical assessment of the fatigue performance of additively manufactured Ti–6Al–4 V and perspective for future research, Int. J. Fatigue 85 (2016) 130–143.

[37] S. Kashef, A. Asgari, T.B. Hilditch, W. Yan, V.K. Goel, P.D. Hodgson, Fatigue crack growth behavior of titanium foams for medical applications, Mater. Sci. Engineering: A 528 (3) (2011) 1602–1607.

[38] R. Hedayati, S.A. Yavari, A. Zadpoor, Fatigue crack propagation in additively manufactured porous biomaterials, Mater. Sci. Engineering: C 76 (2017) 457–463.

[39] R. Hedayati, S. Ahmadi, K. Lietaert, B. Pouran, Y. Li, H. Weinans, C. Rans, A. Zadpoor, Isolated and modulated effects of topology and material type on the mechanical properties of additively manufactured porous biomaterials, J. Mech. Behav. Biomed. Mater. 79 (2018) 254–263.

[40] L.J. Gibson, M.F. Ashby, Cellular solids: Structure and Properties, Cambridge university press, 1999.

[41] R. Wauthle, B. Vrancken, B. Beynaerts, K. Jorissen, J. Schrooten, J.-.P. Kruth, J. Van Humbeeck, Effects of build orientation and heat treatment on the microstructure and mechanical properties of selective laser melted Ti6Al4V lattice structures, Additive Manufacturing 5 (2015) 77–84.

[42] T. Craeghs, S. Clijsters, E. Yasa, F. Bechmann, S. Berumen, J.-.P. Kruth, Determination of geometrical factors in Layerwise Laser Melting using optical process monitoring, Opt. Lasers Eng. 49 (12) (2011) 1440–1446.

[43] S.L. Sing, F.E. Wiria, W.Y. Yeong, Selective laser melting of lattice structures: a statistical approach to manufacturability and mechanical behavior, Robot Comput. Integr. Manuf. 49 (2018) 170–180.

[44] S. Van Bael, G. Kerckhofs, M. Moesen, G. Pyka, J. Schrooten, J.-.P. Kruth, Micro-CT-based improvement of geometrical and mechanical controllability of selective laser melted Ti6Al4V porous structures, Mater. Sci. Engineering: A 528 (24) (2011) 7423–7431.

[45] J. Pegues, M. Roach, R.S. Williamson, N. Shamsaei, Surface roughness effects on the fatigue strength of additively manufactured Ti-6Al-4 V, Int. J. Fatigue 116 (2018) 543–552.

[46] S. Ahmadi, R. Kumar, E. Borisov, R. Petrov, S. Leeflang, Y. Li, N. Tümer, R. Huizenga, C. Ayas, A. Zadpoor, From microstructural design to surface engineering: a tailored approach for improving fatigue life of additively manufactured meta-biomaterials, Acta Biomater. 83 (2019) 153–166.

[47] J. de Krijger, C. Rans, B. Van Hooreweder, K. Lietaert, B. Pouran, A.A. Zadpoor, Effects of applied stress ratio on the fatigue behavior of additively manufactured porous biomaterials under compressive loading, J. Mech. Behav. Biomed. Mater. 70 (2017) 7–16.

[48] S.A. Yavari, S. Ahmadi, R. Wauthle, B. Pouran, J. Schrooten, H. Weinans, A. Zadpoor, Relationship between unit cell type and porosity and the fatigue behavior of selective laser melted meta-biomaterials, J. Mech. Behav. Biomed. Mater. 43 (2015) 91–100.

[49] J. Schijve, Fatigue of Structures and Materials, Springer Science & Business Media, 2001.

[50] S. Tammas-Williams, P. Withers, I. Todd, P. Prangnell, The influence of porosity on fatigue crack initiation in additively manufactured titanium components, Sci. Rep. 7 (1) (2017) 1–13.

[51] S. Tammas-Williams, P.J. Withers, I. Todd, P.B. Prangnell, The effectiveness of hot isostatic pressing for closing porosity in titanium parts manufactured by selective electron beam melting, Metall. Mater. Trans. A 47 (5) (2016) 1939–1946.

[52] B. Van Hooreweder, Y. Apers, K. Lietaert, J.-.P. Kruth, Improving the fatigue performance of porous metallic biomaterials produced by selective laser melting, Acta Biomater. 47 (2017) 193–202.

[53] R. Molaei, A. Fatemi, N. Phan, Significance of hot isostatic pressing (HIP) on multiaxial deformation and fatigue behaviors of additive manufactured Ti-6Al-4 V including build orientation and surface roughness effects, Int. J. Fatigue 117 (2018) 352–370.

[54] E. Maleki, S. Bagherifard, M. Bandini, M. Guagliano, Surface Post-Treatments For Metal Additive manufacturing: Progress, challenges, and Opportunities, Additive Manufacturing, 2020.

[55] S. Bagehorn, J. Wehr, H. Maier, Application of mechanical surface finishing processes for roughness reduction and fatigue improvement of additively manufactured Ti-6Al-4 V parts, Int. J. Fatigue 102 (2017) 135–142.

[56] R. Hedayati, S. Janbaz, M. Sadighi, M. Mohammadi-Aghdam, A. Zadpoor, How does tissue regeneration influence the mechanical behavior of additively manufactured porous biomaterials? J. Mech. Behav. Biomed. Mater. 65 (2017) 831–841.

[57] A.A. Zadpoor, Mechanical performance of additively manufactured meta-biomaterials, Acta Biomater. 85 (2019) 41–59.

[58] S.A. Yavari, R. Wauthlé, J. van der Stok, A. Riemslag, M. Janssen, M. Mulier, J.-.P. Kruth, J. Schrooten, H. Weinans, A.A. Zadpoor, Fatigue behavior of porous biomaterials manufactured using selective laser melting, Mater. Sci. Engineering: C 33 (8) (2013) 4849–4858.

[59] S. Ahmadi, R. Hedayati, Y. Li, K. Lietaert, N. Tümer, A. Fatemi, C. Rans, B. Pouran, H. Weinans, A. Zadpoor, Fatigue performance of additively manufactured meta-biomaterials: the effects of topology and material type, Acta Biomater. 65 (2018) 292–304.